Modulating the electronic properties along carbon nanotubes via tube-substrate interaction

Jaqueline S. Soares,[†] Ana Paula M. Barboza,[†] Paulo T. Araujo,[†] Newton M. Barbosa Neto,[†, //] Denise Nakabayashi,[†] Nitzan Shadmi,[§] Tohar S. Yarden,[§] Ariel Ismach,[§] Noam Geblinger,[§] Ernesto Joselevich,[§] Cecilia Vilani,[⊥] Luiz G. Cançado,[†,#] Lukas Novotny,[#] Gene Dresselhaus,[¥] Mildred S. Dresselhaus,[£] Bernardo R. A. Neves,[†] Mario S. C. Mazzoni,[†] Ado Jorio*[†]

Supporting Information

Materials and Methods

Sample preparation. Carbon nanotubes were grown by catalytic chemical vapor deposition (CVD) on top of one-side polished single-crystal quartz wafers (Sawyer Research Products, Inc.), as discussed in ref. (1). The substrates were cleaned by sonication in acetone. Parallel stripes of amorphous SiO_2 (Kurt J.Lesker, 99.99 %) were laid down in the surface step direction by photolithography and electron-beam evaporation and deposition of 0.5 nm thick evaporated layer of Fe, the growth catalyst, (Kurt J.Lesker, 99.95 %) was evaporated on the amorphous SiO_2 stripes. A lift-off was done by weak sonication in acetone and the Fe particles were oxidized in air. The samples were placed inside the middle of a quartz tube at a defined angle α between the surface steps and the gas flow. The tube was placed in a furnace, and CVD was carried out at 900 °C and 1 atm for 60 min from a mixture of 60 % Ar, 40 % H_2, 0.4 % C_2H_4 at flow rate of 500 sccm (cm^3/min).

Raman spectroscopy. Confocal Raman measurements were performed on an inverted optical microscope with the addition of an x,y-stage for raster-scanning the samples. Light from a He-Ne laser (632.8 nm) is reflected by means of a beam splitter and then focused onto the surface of the sample using an oil-objective with 60× magnification. Having obtained a tight focal spot at the sample surface and using the x,y-scan stage to raster scan the sample, Raman scattered light is collected by the same microscope objective and recorded using either a single-photon counting avalanche photodiode (APD) or a spectrograph with a charged-coupled device (CCD).

Near-field Raman spectroscopy. Near-field Raman spectroscopy from carbon nanotube serpentine samples were obtained using the same system described above, by approaching a gold tip to the sample surface[2]. The near field is obtained through the tip-enhanced Raman scattering (TERS) effect, with a typical tip diameter of 20-40nm and typical sample-tip distance of ~2nm, as described in details in[3].

Atomic Force Microscopy. Detailed atomic force microscopy (AFM) measurements were performed by JPK Nanowizard (JPK Instruments AG) atomic force microscope operating in tapping mode. A cantilever commercially available (Mikromasch 35 NSC/ALBS - nominal constant spring – $k \sim 40$ N/m) was employed for AFM images acquisition.

Electric Force Microscopy. Electric force microscopy (EFM) and joint atomic force microscopy (AFM) measurements were performed by scanning probe microscopy (SPM) (Nanoscope IV MultiMode SPM, from Veeco Instruments). AuCr-covered silicon cantilevers with nominal spring constant $k \sim 0.3$ to 0.6 N/m, nominal radius of curvature $R \sim 30$ nm and resonant frequency $\omega_0 \sim 20$ to

40 kHz were employed throughout this work for AFM (intermittent contact modes) and EFM characterization.

Scanning Electron Microscopy. Scanning Electron Microscopy (SEM) images were taken using field-emission SEM instruments Supra 55VP FEG LEO and Ultra 55 Zeiss, Oberkochen, Germany, at low working voltages of 0.5-2.0 kV.

Supporting Text

First-principles calculations. While theoretical and experimental works have been developed for studying the effect of strain[4-6] and doping[7,8] on ω_G^{LO} and ω_G^{TO}, these published models cannot be directly used here to quantify the effects reported in this study. The published models address strain and doping levels that are much smaller in magnitude than the effects expected for the carbon nanotube-SiO2 substrate interaction[9-12]. This is made evident from the observed shifts in the present work, as compared with previous observations[4-8,13], and confirmed by our own calculations. First-principles calculations were performed within the Pseudopotential Density Functional Theory (DFT)[14-16] formalism as implemented in the SIESTA program[17,18], which makes use of a basis set composed of pseudo atomic functions of finite range. The Generalized Gradient Approximation (GGA) within the Perdew-Burke-Erzerhof (PBE) parametrization[19] was employed for the exchange-correlation functional.

In our geometric models, the nanotube is placed on top of a SiO_2 slab saturated by H atoms at its bottom part. Periodic boundary conditions are used with the vertical lattice vector large enough to prevent interactions between the system and its repetitions. We consider distinct arrangements for the contact region between the nanotube and the slab. We mention, for instance, a contact region with either Si or O atoms exposed with dangling bonds and an intermediate geometry in which only some of the

3

surface O atoms are non-passivated. Outside the contact region, all Si atoms make bonds with –OH groups. These geometries are meant to mimic conditions in which a strong adhesion of the nanotube may take place. Although we can not pinpoint which specific mechanism is responsible for the adhesion (covalent bonds between exposed O or Si atoms with the nanotube or a charge transfer between O atoms and the nanotube), the idea is that the existence of a periodic array of interaction sites (this is the importance of the crystalline quartz) may cause the appearance of dispersive bands crossing the Fermi level. These may be defective bands (dispersive because of the periodicity), if they originate from covalent bonds, or simply a shift of the Fermi level, if charge is transferred from the nanotube to surface atoms (without making additional bonds). The former case is illustrated in Fig. S1, which shows the band structure of an originally semiconductor (19,0) nanotube interacting with a SiO_2 slab having Si dangling bonds, as described in our paper (see Fig. 4 on the main text). Here the system is periodic in both the [100] and [010] directions normal to (100). The lateral lattice vector has a length of 2.6 nm, which is enough to avoid interactions between the nanotube and its periodic repetitions. The ten oxygen atoms at the bottom side of the surface are held fixed to mimic the structural effect of the missing part of the substrate, and they are saturated by hydrogen atoms.

When the nanotube is placed across the surface steps, a strong interaction is supposed to exist only locally, at the steps themselves. The consequence in the band structure would be a set of non-dispersive defective bands, and this is consistent with preliminary efforts we made to calculate such structures. Therefore, the general picture is a significant interaction for tubes aligned along the steps, which may modulate the electronic properties of the nanotube (such as a semiconductor-metal transition evidenced by the presence of dispersive bands crossing the Fermi level in Fig. S1), and localized interactions in the steps, which act as isolated defects in the band structure.

4
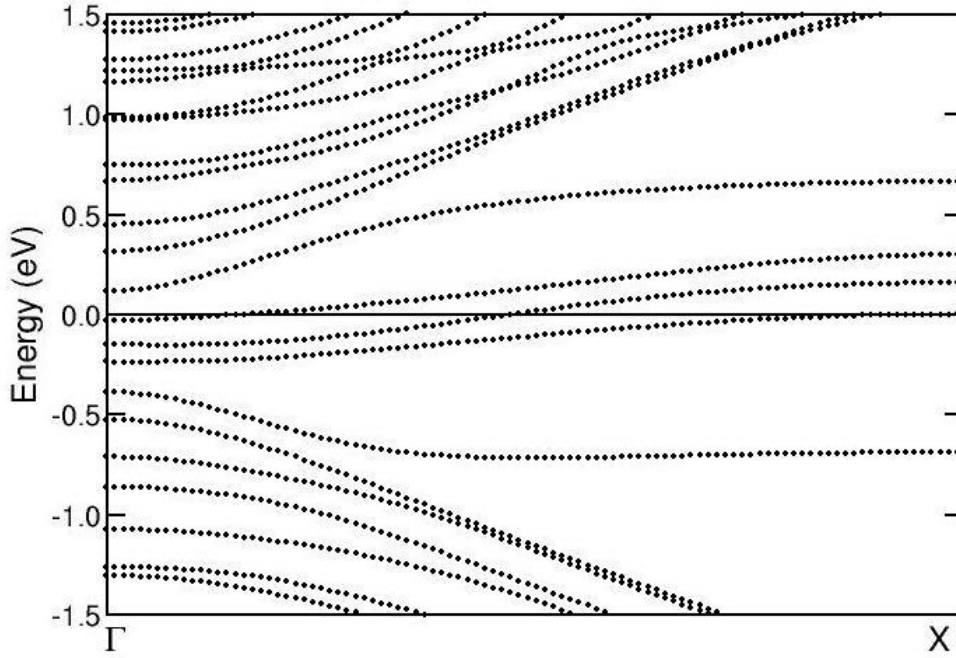
Figure S1: Band structure of the system discussed in Fig. 4 of the main paper, i.e. a (19,0) carbon nanotube interacting with a SiO_2 slab. The Fermi level is set to zero.

Imaging a SWNT serpentine by Scanning Electron Microscopy and Atomic Force Microscopy – The tube growth direction. We have used scanning electron microscopy (SEM) and atomic force microscopy (AFM) in order to fully characterize the SWNT serpentines. Figure S2 shows the SEM and AFM images of the serpentine discussed in our paper. The SEM image shows the markers used to locate the serpentines and the amorphous silicon, where the catalystic particles are deposited, from where the carbon nanotubes grow. The black arrow indicates the serpentine location that is discussed in detail in our paper. Since the tube grows from the large white/gray track in (a), where the catalyst particles are placed, by image magnification we know that the growth direction in Fig. (b) occurred from the bottom-right to the top-left part of the tube displayed. Notice the growth is generally perpendicular to the amorphous Si track, but exactly at the point we measure, there is a shift to the side (to the right in panel

(a) and to the left in panel (b) – the figures are mirror symmetric), probably related to fluctuations in the gas flow direction near the lithographic markers.
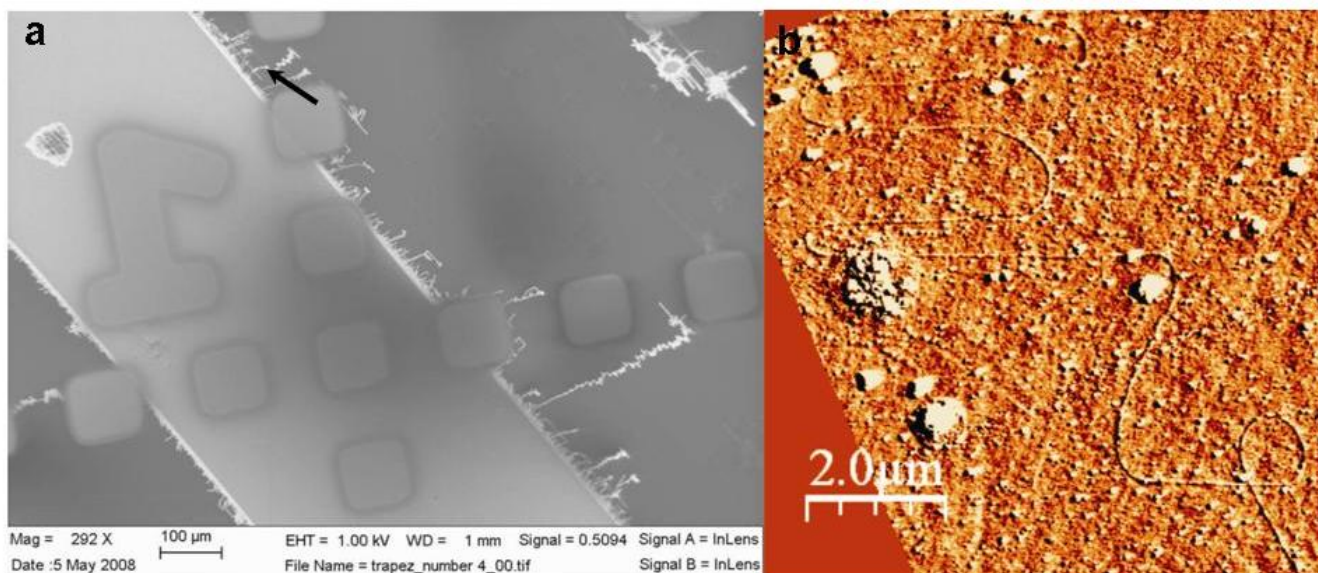
Figure S2: (a) SEM and (b) AFM images of the SWNT serpentine on top of the quartz substrate. The black arrow in the SEM image shows exactly the point where the AFM image in (b) was taken.
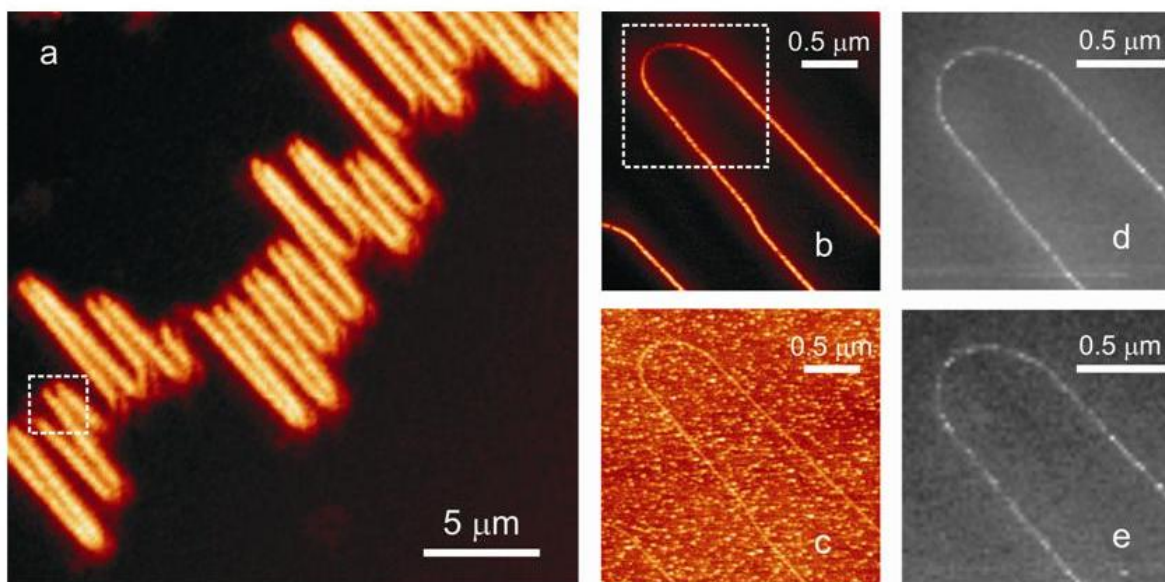
Figure S3: (a) Confocal Raman image corresponding to the *G* band intensity of a carbon nanotube serpentine. (b) Near-field optical Raman image corresponding to the *G* band intensity recorded in the boxed area in panel (a). (c) Topographic image obtained simultaneously with the near-field image shown in panel (b). Panels (d) and (e) show two hyper-spectral Raman images corresponding to the *G* mode and *RBM* intensities, respectively, obtained from the boxed area in panel (b).

Imaging a SWNT serpentine by Near-field Raman Spectroscopy – The tube crystallinity. Near-field scanning optical (NSOM) Raman spectroscopy measurements were obtained from 6 SWNT serpentines to check local effects related by the presence of defects in the tube structure. One example is shown in Fig.S3. The spectra quality indicates an unusually high crystallinity of the samples, with no local emission characteristics of defects, usually identified by the presence of a Raman peak in the 1300-1400 cm^{-1} spectral range, known as the D band (see also ref. 2), or a localized variation in the intensity of allowed Raman peaks (G and RBM)[20,21]. Huang and Choi[22] observed that the length-normalized resistance of carbon nanotube serpentines increase with the number of U-turns, and such behavior was explained by the presence of defects in the curved regions. Our metal-semiconductor junctions can explain the results observed in ref. (22) with perfectly crystalline junctions, where the "defects" would be the substrate changing the tube electronic behavior. This is supported by our Raman spectroscopy results with the complete absence of the disorder-induced D-band peak (~1300 cm^{-1}), which is normally observed in defective sp^2 carbon materials[23]. Notice this serpentine has an RBM, but as discussed in the next topic of this supporting online material, an RBM based (*n,m*) assignment is not yet clear for our SWNTs on quartz. The high crystallinity reported here was also observed for SWNT serpentines where no RBM emission was observed.

7

Comment about D-band mode. Clearly our SWNTs are distinct by the complete absence of the defect induced D-band. Considering the work from different collaborators, we know by now studies on 41 SWNT serpentines grown by the group of Ernesto Joselevich, and none of these serpentines exhibited a D-band, while all of them show important changes on G and G′ bands. In some cases the samples are dirty (see Figure S2b), but still, the presence of impurities on top of the SWNT serpentines do not cause a D-band in their Raman spectra. You can even press these SWNT serpentines with AFM tips while acquiring the Raman spectra, and usually no D band is seen. We do see a very small D peak in areas where we clearly caused some damage with the AFM tip (such studies have been performed in our laboratory and will be reported in the near future).

Considerations about the radial breathing mode. The authors are aware that the RBM is a very useful signature for SWNTs, including for assigning the metal vs. semiconducting character. However, we understand that the observation of the RBM, in the present study, is neither a proof of isolated tubes (since another non-resonant SWNT could be bundling with the measured SWNT), nor a proof of the metallic vs. semiconducting character of the tube, since the substrate-induced distortions may be significant, i.e. significant frequency changes or RBM quenching are expected. From the 9 serpentines we measured, 6 of them have RBM modes, and the RBMs, involving atomic displacements normal to the plane of the substrate, are always unchanged along the whole serpentines. From the 4 SWNTs exhibiting the metal-semiconducting hybrid behavior, only one of them has an observable RBM, but the RBM-based (*n,m*) analysis, or even the metal vs. semiconducting assignment, is not clear from a Kataura plot based analysis[24]. The same holds for the other 5 cases where no metal-semiconducting hybrid behavior is observed. Here we base our metal vs. semiconducting assignment on the G band analysis. The physics behind this peak is now well developed and surpasses the structural information delivered by the RBM with respect to metallic vs. semiconducting character. Nevertheless, we are now

developing a Kataura plot based RBM analysis for tubes on the quartz substrate, and strong deviations from the established RBM frequencies and optical transition energies seem to apply.

Comment about the measurements in other SWNT serpentines. As mentioned in the main text, we measured 9 SWNT serpentines and significant tube-substrate interaction could be identified in all of them. The formation of alternating metal-semiconductor behavior has been observed in 4 cases. In 4 other serpentines, we measured a semiconductor SWNT behavior all over the tubes. We also measured one SWNT serpentine with a metallic character.

Figure S4 shows the G band Raman spectra of two SWNT serpentines, one with a semiconducting character, shown in Fig. S4a, and another with a metallic character, shown in Fig. S4b. Both G band spectra change when changing location along the serpentine. The G^+ peak for semiconducting case shifts to higher frequencies when the tube is along the substrate steps (Fig. S4a top) and the G^- peak for the metallic tube shifts to lower frequencies when the tube is along the substrate steps (Fig. S4b bottom). These changes show the tube-substrate interaction and modulation in other SWNT serpentines, and we find the spectra taken on different serpentines to be qualitatively consistent with observations in the paper.
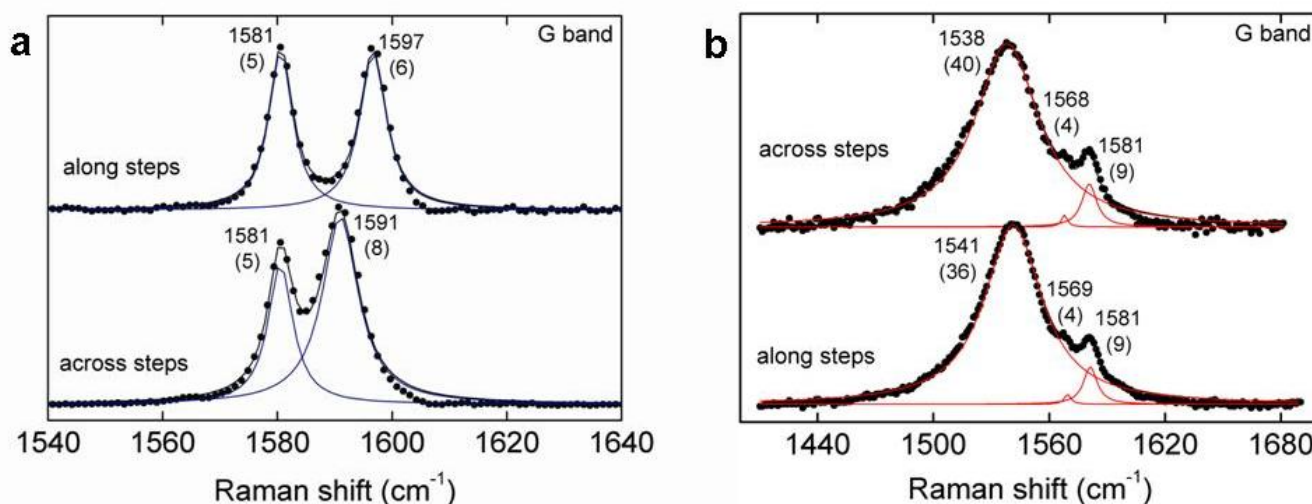
Figure S4: Spectroscopic analysis of two SWNT serpentines grown on quartz. Spectrum (a) exhibits a G band with a lineshape typical of a semiconducting SWNT. Spectrum (b) exhibits a G band with a lineshape typical of a metallic SWNT (see text).

Direct determination of the metallic/semiconducting character of a SWNT via Electric Force Microscopy (EFM) imaging. The determination of metallic vs. semiconducting character of a SWNT using EFM has been demonstrated and reported recently.[27] Here we provide a schematic for a clear understanding of the effect (see Fig.S5). The EFM measures the dielectric response of the whole sample, i.e. SWNT plus substrate. In general, when the tip approaches the dielectric material, there is a decrease in $\Delta\omega$. Then two effects happen in our measurement, as depicted in Fig.S5: (1) $\Delta\omega$ decreases when the tip approaches the tube, reaches a minimum when at the top of the tube, and increases back when the tip departs from the tube (see column a in Fig.S5); (2) $\Delta\omega$ shows a slight increase during the constant-height scan, because the EFM tip retracts when crossing the tube (see column b in Fig.S5). The change in surface-tip distance causes a lowering in the tip-substrate interaction. The overall result is a sum of these two effects (see column c in Fig.S5). In the case of semiconducting SWNT (blue), when the EFM tip is really going on top of the tube, the tip retraction due to change in surface height causes a lowering in the tip-substrate interaction, giving rise to the "W shaped" in the semiconducting SWNTs. This effect is indeed present in the metallic SWNT (red), but not observable due to the different (stronger and sharper) dielectric response, thus keeping a slightly distorter "V shaped" EFM profile.
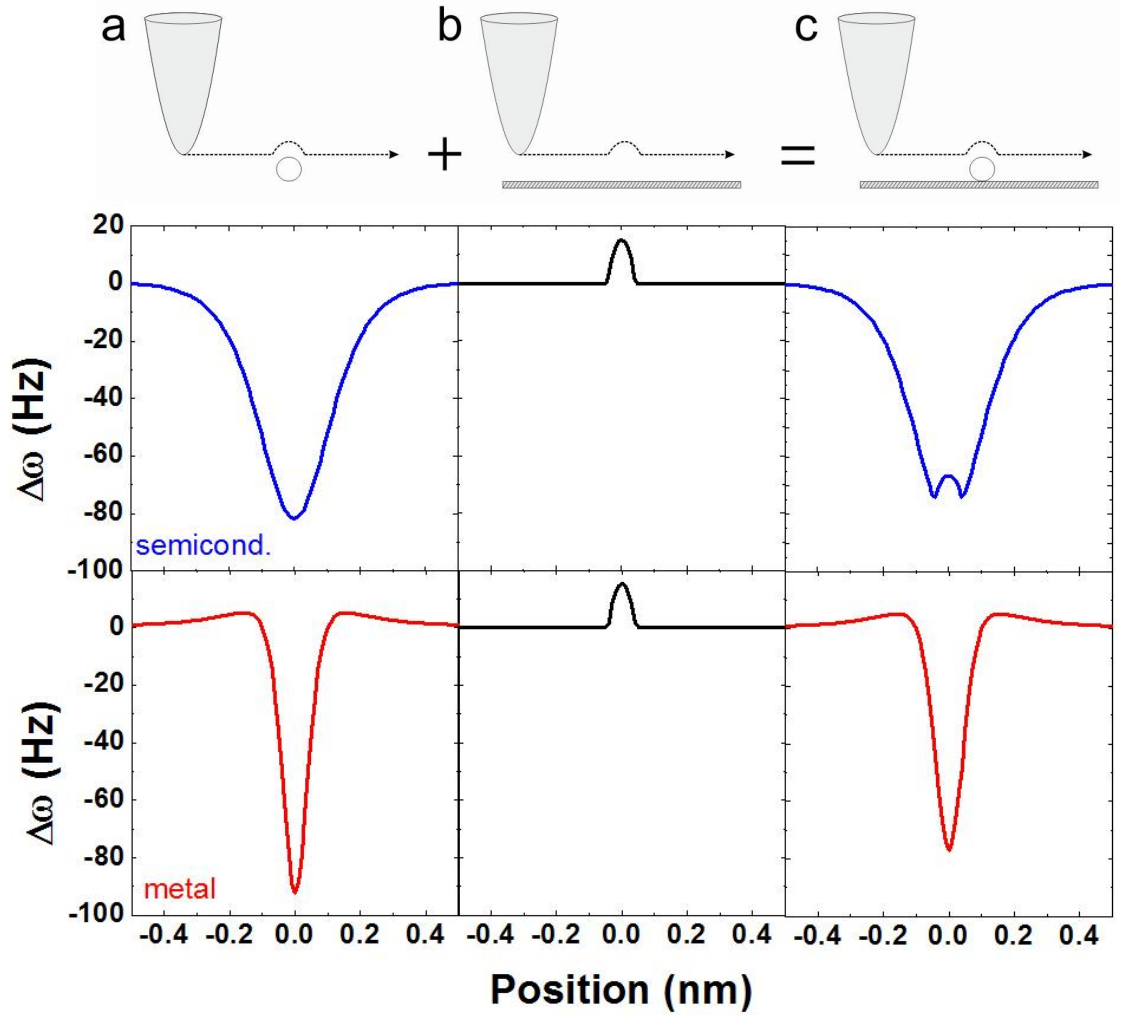
Figure S5: The EFM profiles for semiconducting and metallic SWNTs. In column (a), the effect of the EFM tip crossing a semiconductor (blue) and a metallic (red) SWNTs on Δω are shown. The lineshapes are different due to the differences in dielectric response. In column (b) the effect of the EFM tip retracting from the substrate on Δω are shown. Here the effect is the same for both semiconductors and metals. In column (c) the two effects are combined. The plots shown here were built using the equations in ref. (*27*).

Besides the case study in the main paper, we also have SWNT serpentines that are only metallic or only semiconducting in our samples. Here we show the EFM and G band Raman measurements

performed in SWNT serpentines that are only metallic and only semiconducting (see Figures S6 and S7, respectively). The EFM results are self consistent and consistent with the Raman spectroscopy results.
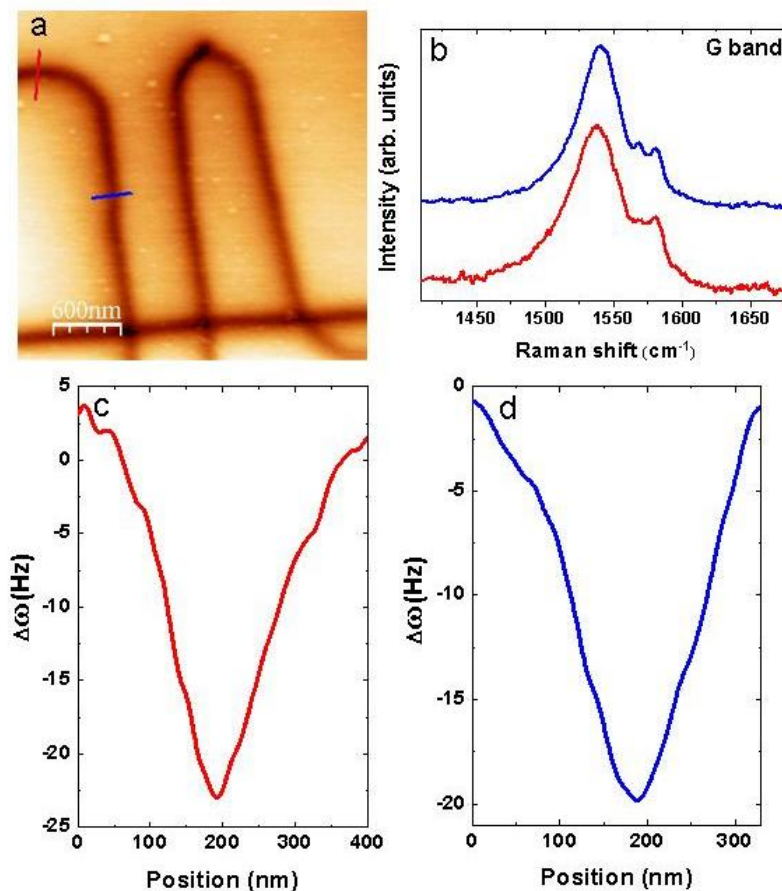
Figure S6: Analysis of a metallic SWNT serpentine grown on quartz. (a) EFM image of the metallic SWNT serpentine. The red and dark blue lines indicate the two regions where the Raman spectra in (b) and the Δω profiles in (c) and (d) were acquired. (b) Raman spectra of the metallic SWNT serpentine in the straight segment (blue) and at the edge of the U turn (red). (c) and (d) EFM scan across the metallic SWNT at the edge of the U turn (c) and in the straight segment (d). The Δω "V" shaped line profile shows the EFM signal characteristic of metallic tubes.
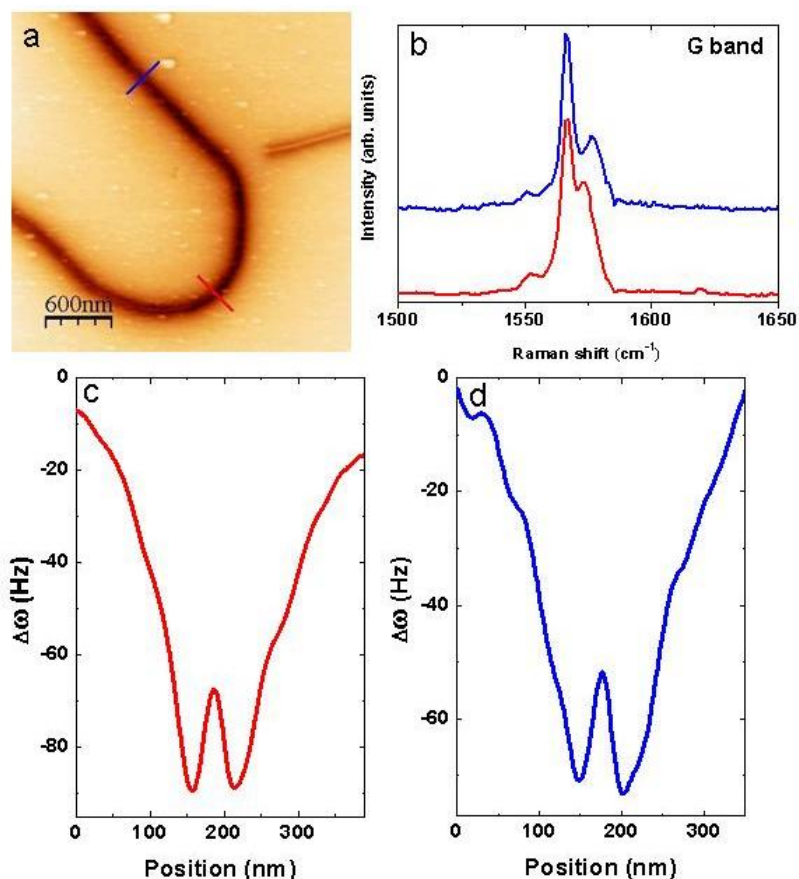
Figure S7: Analysis of a semiconducting SWNT serpentine grown on quartz. (a) EFM image of the semiconducting SWNT serpentine. The red and dark blue lines indicate the two regions where the Raman spectra in (b) and the Δω profiles in (c) and (d) were acquired. (b) Raman spectra of the semiconducting SWNT serpentine in the straight segment (blue) and at the edge of the U turn (red). (c) and (d) EFM scan across the semiconducting SWNT at the edge of the U turn (c) and in the straight segment (d). The Δω "W" shaped line profile shows the EFM signal characteristic of semiconducting tubes.

References

(1) Geblinger, N.; Ismach, A.; Joselevich, E. *Nature Nanotech.* **3**, 195-200 (2008).

(2) Cancado, L. G.; Jorio, A.; Ismach, A.; Joselevich, E.; Hartschuh, A.; Novotny, L. *Phys. Rev. Lett.* **103**, 186101 (2009).

(3) Cancado, L. G.; Hartschuh, A.; Novotny, L. *J. Raman Spec.* **40**, 1420-1426 (2009).

(4) Cronin, S. B.; Swan, A. K.; Ünlü, M. S.; Goldberg, B. B.; Dresselhaus, M. S.; Tinkhan, M. *Phys. Rev. Lett.* **93**, 167401 (2004).

(5) Duan, X.; Son, H.; Gao, B.; Zhang, J.; Wu, T.; Samsonidze, Ge. G.; Dresselhaus, M. S.; Liu, Z.; Kong, J. *Nano Lett.* **7**, 2116-2121 (2007).

(6) Gao, B.; Jiang, L.; Ling, X.; Zhang, J.; Liu, Z. *J. Phys. Chem. C* **112**, 20123-20125 (2008).

(7) Das, A.; Sood, A. K.; Govindaraj, A.; Marco Saitta, A.; Lazzeri, M.; Mauri, F.; Rao, C. N. R. *Phys. Rev. Lett.* **99**, 136803 (2007).

(8) Tsang, J. C.; Freitag, M.; Perebeinos, V.; Liu, J.; Avouris, PH. *Nature Nanotech.* **2**, 725-730 (2007).

(9) Orellana, W.; Miwa, R. H.; Fazzio, A. *Phys. Rev. Lett.* **91**, 166802 (2003).

(10) Miwa, R. H.; Orellana, W.; Fazzio, A. *Appl. Phys. Lett.* **86**, 213111 (2005).

(11) Berber, S.; Oshiyama, A. *Phys. Rev. Lett.* **96**, 105505 (2006).

(12) Peng, G. W.; Huan, A. C. H.; Liu, L.; Feng, Y. P. *Phys. Rev. B* **74**, 235416 (2006).

(13) Steiner, M.; Freitag, M.; Tsang, J. C.; Perebeinos, V.; Bol, A. A.; Failla, A. V.; Avouris, PH. *Appl. Phys. A* **96**, 271-282 (2009).

(14) Kohn, W.; Sham, L. J. *Phys. Rev.* **140**, A1133- A1138 (1965).

(15) Kleinman, L.; Bylander, D. M. *Phys. Rev. Lett.* **48**, 1425-1428 (1982).

(16) Troullier, N.; Martins, J. L. *Phys. Rev. B* **43**, 1993-1996 (1991).

(17) Ordejón, P.; Artacho, E.; Soler, J. M. Phys. Rev. B **53**, R10441- R10444 (1996).

(18) Soler, J. M.; Artacho, E.; Gale, J. D.; García, A.; Junquera, J.; Ordejón, P.; Sánchez-Portal, D. *J. Phys.: Condens. Matter* **14**, 2745-2779 (2002).

(19) Perdew, J. P.; Burke, K.; Ernzerhof, M. *Phys. Rev. Lett.* **77**, 3865-3868 (1996).

(20) Anderson, N.; Hartschuh, A.; Cronin, S.; Novotny, L. *J. Am. Chem. Soc.* **127**, 2533-2537 (2005).

(21) Maciel, I. O.; Anderson, N.; Pimenta, M. A.; Hartschuh, A.; Qian, H.; Terrones, M.; Terrones, H.; Campos-Delgado, J.; Rao, A. M.; Novotny, L.; Jorio, A. *Nature Mat.* **7**, 878-883 (2008).

(22) Huang, J.; Choi, W. *Nanotechnology* **19**, 505601 (2008).

(23) Dresselhaus, M. S.; Dresselhaus, G.; Saito, R.; Jorio, A. Phys. Rep. 409, 47-99 (2005).

(24) Araujo, P. T.; Pesce, P. B. C.; Dresselhaus, M. S.; Sato, K.; Saito, R.; Jorio, A. *Physica E* **42**, 1251-1261 (2010).

(25) Bonnell, D. A. *Scanning Probe Microscopy and Spectroscopy* (Wiley-VCH, New York, 2001).

(26) Barboza, A. P. M.; Gomes, A. P.; Archanjo, B. S.; Araújo, P. T.; Jorio, A.; Ferlauto, A. S.; Mazzoni, M. S. C.; Chacham, H.; Neves, B. R. A. *Phys. Rev. Lett.* **100**, 256804 (2008).

(27) Barboza, A. P. M.; Gomes, A. P.; Chacham, H.; Neves, B. R. A. *Carbon* **48**, 3287-3292 (2010).